JVST A
Journal of Vacuum Science & Technology A

ARTICLE

avs.scitation.org/journal/jva

Numerical ellipsometry: A method for selecting a near-minimal infrared measurement set for β-gallium oxide

Cite as: J. Vac. Sci. Technol. A **39**, 052801 (2021); doi: 10.1116/6.0001002
Submitted: 25 February 2021 · Accepted: 7 June 2021 ·
Published Online: 7 July 2021

Frank K. Urban III,[1,a)] David Barton,[1] and Mathias Schubert[2]

AFFILIATIONS

[1]Department of Electrical and Computer Engineering, Florida International University, University Park Campus, Miami, Florida 33199
[2]Department of Electrical and Computer Engineering, University of Nebraska Lincoln, 242N Scott Engineering Center, Lincoln, Nebraska 68588-0511

Note: This paper is part of the Special Topic Collection on Gallium Oxide Materials and Devices.
[a)]**Electronic mail:** urban@fiu.edu

ABSTRACT

The objective of this work is to develop a method for defining, *a priori*, a set of minimum ellipsometry measurements that provide for a near-minimal data set (measurement set) sufficient for an analysis of optically anisotropic crystals with monoclinic symmetry with minimal prior knowledge. Example measurements are obtained by reflection from two differently oriented smooth, flat, anisotropic, monoclinic β-Ga_2O_3 crystals. A measurement may consist of any set of common type ellipsometry data such as selected sets of normalized Jones matrix elements or selected sets of normalized Mueller matrix elements measured at selected angles of incidence and/or rotation of the sample, also know as table rotation. The only prior knowledge used here is the crystallographic surface orientation. The four complex-valued permittivity parameters of the monoclinic symmetry crystal are then the object of interest and the only remaining unknown parameters. The motif for our investigation is the desire to better understand how to reduce measurement time for the otherwise extensive data acquisition considered necessary thus far to fully characterize low-symmetry anisotropic materials in substrates and semiconductor heterostructures. The near-minimal measurement set introduced here is then obtained by selection from a prior, larger data set. The larger data set thus far largely overdetermines the amount of necessary information. The first criterion is that there be sufficient intensity of the reflected light considering the p and s polarized reflections produced by p and s polarized incident light. The second criterion for inclusion is that the permittivity tensor is sensitive to measurement, that is, a significant change in a measurement set results in a significant change in the solution for permittivity. Finally, the near-minimal measurement set must result in solvable sets of equations. This is examined by computing the Jacobian of the system of equations for various sets of measurements in order to only keep measurements for which the condition of the Jacobian falls below the threshold for usability. We find that sets containing four measurements of on-diagonal Jones matrix elements alone, obtained across a wide spread of table rotations, provide most sensitive and intrinsically sufficient information to solve for the permittivity values. In summary, the scheme consists of determining the following measurement conditions: (1) reflections of high intensity to enable accurate measurements. (2) sensitivity to the unknown parameters, and (3) a solvable set of equations.

I. INTRODUCTION

Ellipsometry is a method used to determine the optical properties of a sample from measurements of the change in the polarization state of light reflected from or transmitted through it. Anisotropic optical materials possess properties that depend upon propagation direction. One example is the topic of this work, optically nondepolarizing single crystals of monoclinic β-Ga_2O_3. The part of the spectrum under examination here is in the infrared from a dataset ranging from 300 to 1100 (1/cm) wave numbers, which corresponds to a wavelength ranging from 33×10^3 to 9.1×10^3 nm.

Work on methods of formulating Maxwell's equations for a convenient reflection or transmission geometry has been carried out by a number of authors referenced in our earlier paper.[1–5] The formalism used here was originally published by Berreman, who treated the case of plane polarized light incident on a reflecting/transmitting sample with example cases of vertically homogeneous and inhomogeneous biaxial anisotropy.[1]

More recent work by the authors and the work here found that the permittivity tensor of monoclinic β-Ga_2O_3 across a range of wavenumbers may not be always diagonalizable by a single angle of rotation, in agreement with Jellison *et al.*[6] Prior measurements were made at five azimuths (table rotations) and three incidence angles on two different crystal orientations. The permittivity model consists of a sum of line-broadening terms plus high frequency contributions to provide fitted mode wavenumbers, amplitudes, and line widths for modes of the crystal. More detail is provided in the cited publications.[7]

Recent interest in crystalline materials with monoclinic symmetry is a result of their potential for application in, for example, electronic power devices, scintillators, high-power lasers, frequency stable laser local oscillators, light slowing and trapping devices, and optical quantum memory technologies.[8–14] Of particular interest here is the monoclinic phase (β) of gallium oxide (β-Ga_2O_3), which is thermodynamically stable and can be grown by bulk and epitaxial methods.[9] β-Ga_2O_3 promises potential for application in switches and transistors capable of operating at ten thousand or more volts and large-current-carrying capacities.[9] Thereby, β-Ga_2O_3 may become a transformational competitor for currently envisioned technologies based on silicon carbide and gallium nitride and may hasten the transition to electric mobility as well as the solid-state device enabled transport of electric power.

The goal of the work presented here is to identify near-minimum-number preferred measurements selecting from possible measurements at various incidence angles, sample azimuths (table rotations), and crystal surface-cut orientations in order to significantly reduce the number of required ellipsometry measurements and at the same time improve solution accuracy. This has been addressed by providing methods to identify measurement conditions yielding reflections of high intensity, sensitivity to the unknown parameters, and a solvable set of equations.

The measurement time is an issue at infrared wavelength due to an inconvenience of high intensity sources such as synchrotron beam lines and long integration times for conventional sources-detector combinations such as globar (thermal) source and pyroelectric detection. For example, the data set evaluated in Schubert *et al.* obtained with commercially available instrumentation required approximately two months of nonstop data acquisition. While computation alone can be speeded up most certainly in various ways, the question is not how fast a computer can be; instead the question is, how long one is able to wait to measure sufficient sets of data.

II. THEORY

A. Reflection model

The ellipsometry method and mathematics for the light reflection are well described elsewhere.[1–5] For the present discussion, the derivation of Berreman is used.[1] This is based on the Maxwell equations and a selected geometry for the reflection, which result in expressions relating the reflection to the permittivity of the reflecting surface. For measurements, the coordinate system of the reflecting surface defines the XY plane, which places the Z direction perpendicular to the reflecting surface. We refer to this Cartesian system as the ellipsometer coordinate system.

The incident light causes a reflection from the crystal that can be solved by considering the boundary conditions between the surrounding medium and the crystal. The measured parameters are computed from these computed reflections. This model provides the necessary mathematical relationship between known parameters including the light incidence angle, light wavelength, light reflection measurements, crystal orientation, and the sought-for unknown parameters consisting of the values of the crystal permittivity tensor. More detail is provided by Berreman.[1] In this simple model, a two-phase, anisotropic substrate–isotropic ambient model is created, where no surface overlayers are considered. Surface overlayers are required often to account for the effects of small-scale roughness, e.g., due to polishing processes and/or surfactants but which are irrelevant at infrared wavelengths due to the smallness of their effective optical thickness.

B. Permittivity model

Describing the permittivity in terms of contributions from different physical processes within the crystal provides useful insight. These equations are required to clarify the contributions of the physical processes to the total permittivity, especially phonon resonances appearing following the summation symbol. They cover beyond IR and are expressed by Schubert as follows:

$$\varepsilon_{xx} = \varepsilon_{\infty,xx} + \sum_{j=1}^{8} \rho_j^{B_u} \cos^2\alpha_j + \rho_{FCC,x}, \tag{1a}$$

$$\varepsilon_{xy} = \varepsilon_{\infty,xy} + \sum_{j=1}^{8} \rho_j^{B_u} \sin\alpha_j \cos\alpha_j, \tag{1b}$$

$$\varepsilon_{yy} = \varepsilon_{\infty,yy} + \sum_{j=1}^{8} \rho_j^{B_u} \sin^2\alpha_j + \rho_{FCC,y}, \tag{1c}$$

$$\varepsilon_{zz} = \varepsilon_{\infty,zz} + \sum_{k=1}^{4} \rho_k^{A_u} + \rho_{FCC,z}, \tag{1d}$$

$$\varepsilon_{xz} = \varepsilon_{zx} = 0. \tag{1e}$$

The tensor is expressed, thus,

$$\varepsilon = \begin{bmatrix} \varepsilon_{xx} & \varepsilon_{xy} & 0 \\ \varepsilon_{yx} & \varepsilon_{yy} & 0 \\ 0 & 0 & \varepsilon_{zz} \end{bmatrix}, \tag{2}$$

here $\varepsilon_{\infty,xx}$ terms represent the sum of all higher-energy electronic

band-to-band transitions; $\rho_j^{B_u}$ terms are the mode strength for B_u modes $j = 1–8$; α_j is the angular orientation of the B_u modes j; $\rho_{FCC,x}$ is the free charge carrier for directions x, y, and z; and $\rho_k^{A_u}$ terms stand for the mode strength of A_u modes $k = 1–4$.

There are three kinds of components to each of the terms, except for (1e). Equations (1a)–(1d) have an initial term of high frequency contributions and a second term that consists of a sum of phonon contributions at particular wavenumbers that consist of eight B_u contributions for (1a)–(1c) and four A_u contributions for (1d). Equations (1a), (1c), and (1d) finish with charge carrier contributions. Anisotropy is shown explicitly with the sign and cosine functions in the first three equations and implicitly in the fourth. All of the remaining terms may be anisotropic as well, expressed implicitly here and explicitly in the solutions. A more detailed description is given by Schubert *et al.*[7]

Because measurements were taken on crystals of known orientation, the face that is parallel to the x–y measurement plane is known and, therefore, not solved. Solutions for different table rotations, about measurement z, include the on-diagonal terms that can be transformed by a rotation to near diagonal. Each rotation depends on the wavenumber and so it is more convenient to choose a single z-rotation and include the resulting $xy = yx$ tensor values. Thus, there are four complex unknowns per wavenumber.

C. Crystal

As shown in Fig. 1, the monoclinic crystal may be described in terms of a unit cell with a set of three axes (a, b, and c) and three angles between the axes (α, β, and γ) for which $\gamma = 90°$ is the angle between a and b, $\alpha = 90°$ is the angle between b and c, and $\beta \neq 90°$ lies between a and c. Thus, the b axis is normal to both the a and c axes, and, as a consequence, b is normal to the plane defined by a and c. The only axis of symmetry is b, and there is mirror symmetry in a–c.[7]

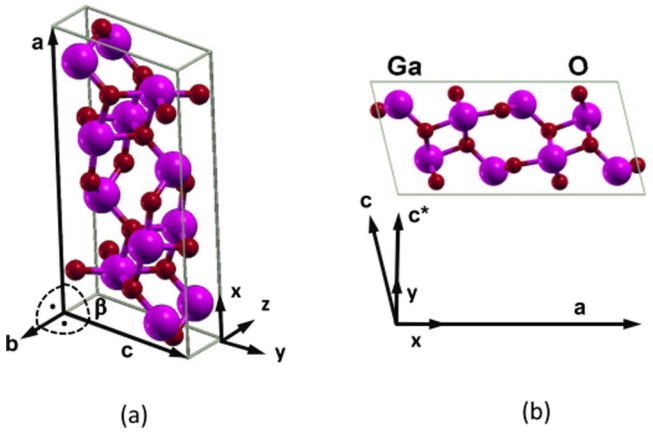

FIG. 1. (a) Unit cell of monoclinic β-Ga_2O_3 with crystal axes a, b, and c. The angles between a and b as well as b and c are 90°. The angle, β, between c and a is greater than 90°. The axes (x, y, and z) represent the instrument axes with the crystal oriented with the a–c plane parallel to the instrument table, the x–y plane. The crystal axis b is aligned with the instrument z axis and pointing downward into the table. (b) The same crystal as (a) but reoriented to more clearly show the a–c plane. Reprinted from Ref. 7.

Incident light in the wavenumber spectrum under investigation excites both electrons and phonons. The phonons are due to oscillations of crystal atom dipoles corresponding to regularly spaced planes that interact together with the incident light. The spectroscopic optical measurements in prior work elucidate the results of this light–material interaction as expressed by the permittivity as a function of the wave number. Specific features in the spectra of measured ellipsometric data are established by the physics of the photon–phonon, photon–electron, and any other interactions in the crystal. The focus of this work is to identify a near-minimum set of measurements to provide for the spectral solution of the permittivity tensor due to all such interactions, paying particular attention to the photon–phonon interactions that occur in the measured wavenumber range.

It is important that we address a point here concerning coordinate system orientations of the permittivity axes (x, y, and z) fixed in the crystal and also fixed in the crystal axes (a, b, and c) (see Fig. 1). First, let us consider the representation of the ε tensor with respect to the crystal axes. The general permittivity tensor for a monoclinic crystal for which we solve is expressed relative to the permittivity axes as

$$\varepsilon = \begin{bmatrix} \varepsilon_{xx} & \varepsilon_{xy} & 0 \\ \varepsilon_{yx} & \varepsilon_{yy} & 0 \\ 0 & 0 & \varepsilon_{zz} \end{bmatrix}.$$

The tensor is symmetric so that $\varepsilon_{xy} = \varepsilon_{yx}$. We refer to this representation as the standard reference tensor consisting of diagonal values and an off-diagonal value. Here, the b crystal axis corresponds to the z direction (ε_{zz}) and the x direction (ε_{xx}) is aligned with the a crystal direction. Thus, the remaining axis (y) is not aligned with the c crystal axis but with an axis c^* instead, as the angle between a and c is not orthogonal but rather 103.7°.[7] Physical rotation of the crystal with respect to the measurement axes requires that the standard reference tensor be rotated appropriately, mathematically, for the model orientation to correspond to the physical orientation.

Because each mode corresponds to a dipole oscillation, it is clear that the exciting electric field at the appropriate frequency must have a component (or generate a component) in a direction capable of influencing the mode dipole. Consequently, not all combinations of light incidence angles, crystal orientations (with respect to the measurement axes), and sample rotations (azimuths) are equally capable of exciting a given mode. This is more extensively described in our prior work.[15]

III. EXPERIMENT

A. Crystals

Substrates of different crystallographic orientations, (010) and (−201), were cut from the bulk crystals and then polished on one side and oriented within a few tenths of a degree. The resulting samples were $10 \times 10\ mm^2$ with a thickness of 0.65 mm.

The substrates were doped with Sn to an estimated activated electron density of $N_d - N_a \approx (2–9) \times 10^{18}$ cm^{-3}.

As is shown in the prior work and the present work, there is not a general principal axis that exists across the wave number spectrum; rather there are many phonon modes at various angles within the crystal. Therefore, it is not possible to prepare the crystal such that all modes can be specially aligned for measurement. All samples are analyzed by XRD prior to shipping from the manufacturer (Novel Crystal Technologies, Tokyo, Japan, a spinoff of the Tamura Corp.). The crystals were cut under specified angles from ingots obtained by the edge-defined film-fed growth (EFG) process.[16] It is noted that crystal axes *a* and *c* are not associated with specific signatures within far infrared and infrared optical responses of monoclinic gallium oxide, and angles obtained from ellipsometry analysis are offset information relative to the directions resulting from a particular sample cut. This is due to the fact that there are no principal optical axes identifiable within the monoclinic plane, as noted immediately above. The only axis that can be identified accurately from optical data analysis is axis *b*, which is perpendicular to the monoclinic plane. The orientation angles obtained in the ellipsometry analysis for axis *b* are in full agreement with the XRD data information of the two samples. The samples investigated are surface cuts that are of particular research interest for the growth of homoepitaxial and heteroepitaxial layers in order to develop and test electronic devices for high-power applications. Presently, for example, best quality growth is obtained on (010) substrates, and (010) and (−201) are being discussed and investigated here.

B. Measurements

The original measurements by Schubert *et al.* were made across two different spectral ranges using two different ellipsometers. For the range from 500 to 1500 (1/cm), measurements were performed using a commercial infrared ellipsometer (J. A. Woollam Co., Inc. IR-VASE model) instrument, which is a rotating compensator type with a spectral resolution of 2 (1/cm). Far-infrared measurements in the range of 50–500 (1/cm) were performed on a custom-built rotating-polarizer, rotating-analyzer far-infrared ellipsometer with an average spectral resolution of 1 (1/cm). Measurements were performed at 50°, 60°, and 70° angles of incidence. All measurements were taken directly from data files output from the ellipsometer. The Ψ and Δ numbers were not derived by us but taken directly from the instrument. Both generalized ellipsometry measurements and Mueller matrix measurements were reported. The Mueller matrix is defined by connecting the incident and exiting Stokes vector components as usual.

The ultimate measurement is performed perhaps with the photocurrent of a photosensitive detector depending on the instrumental design. Analog-digital conversion and CMOS based operation amplifiers have moved this original measurement already to a level expressed entirely by ones and zeros. This digital information is then stored versus instrument operation variables such as motor positions, beam splitter location, and other factors and eventually, known equations (entirely always in the Stokes vector component notation because of the dealing with intensity data here) that are used to derive (a) Mueller matrix elements and/or (b) Jones matrix elements, and/or (c) N, C, and S parameters, and/or (d) Ψ and Δ for example. These derivations can be done in multiple ways, for example, matrix inversion, or, as in our case in the J. A. Woollam IRSE, via nonlinear regression, a parameter fit. In this fit, every target data point (intensity vs instrument variable) has a systematic uncertainty obtained only from repeated measurements, termed revolution. Thus, Mueller matrix data, Ψ, Δ, or any other parameters are fit parameters. The "systematic" errors reported in addition are then the numerical regression parameter uncertainties. There is no nonlinear analytic function transformation of measurement to reported parameters. In this sense, none of the reported data in an ellipsometry instrument are, indeed, measured but instead perhaps better be termed "measured." From this point then the general understanding is that the quotation marks are omitted throughout. Therefore, we consider Ψ and Δ as measured values, just as well as their error bars are measured values. We also consider any Mueller matrix reported values and their errors as measured values in a similar fashion.

The generalized ellipsometry parameters are simply defined in terms of Jones matrix elements in reflection,

$$r_{pp}/\, r_{ss} = \rho_{pp} = \tan \Psi_{pp} \exp(i\Delta_{pp}), \tag{3a}$$

$$r_{ps}/r_{pp} = \rho_{ps} = \tan \Psi_{ps} \exp(i\Delta_{ps}), \tag{3b}$$

$$r_{sp}/\, r_{ss} = \rho_{sp} = \tan \Psi_{sp} \exp(i\Delta_{sp}). \tag{3c}$$

Not all Mueller measurements were possible due to the lack of a compensator. Measurements were made on two differently cut surfaces of β-Ga_2O_3 and for four different table rotations (azimuth positions). A subset of Schubert's measurements was used here ranging from 300 to 1100 (1/cm) wavenumbers on two crystals, (010) and (−201), and at four table rotations (azimuths), namely, 0°, 45°, 90°, and 135° and at incidence angles of 50°, 60°, and 70°.

Errors in the measurements due to instrumental factors arise and are reported along with the measurements as estimated experimental errors. Figure 2 shows an example of estimated experimental errors for Mueller matrix components obtained from the (010) crystal at a table rotation of 0°. It can be seen in the figure that the reported Mueller matrix measurements exhibit very large reported estimated experimental errors. These large errors are not substantially different for the three angles of incidence. In addition, measurements at different table rotations and for the other crystal also exhibit these large estimated experimental errors.

A corresponding set of estimated experimental errors for generalized measurements performed on the (010) crystal with no table rotation is shown in Fig. 3. These measurements were taken at the same time as the Mueller matrix measurements. It can be seen in the figure that the best accuracy, small estimated experimental errors are found in the pp terms, i.e., in the ratio of the generalized ellipsometry parameters obtained by dividing the diagonal elements of the Jones matrix.

A careful examination of the measured data in comparison with Figs. 2 and 3 shows that only a few generalizations can be made. The first is that the percent error in both Mueller and generalized (Jones) measurements grows dramatically and consistently

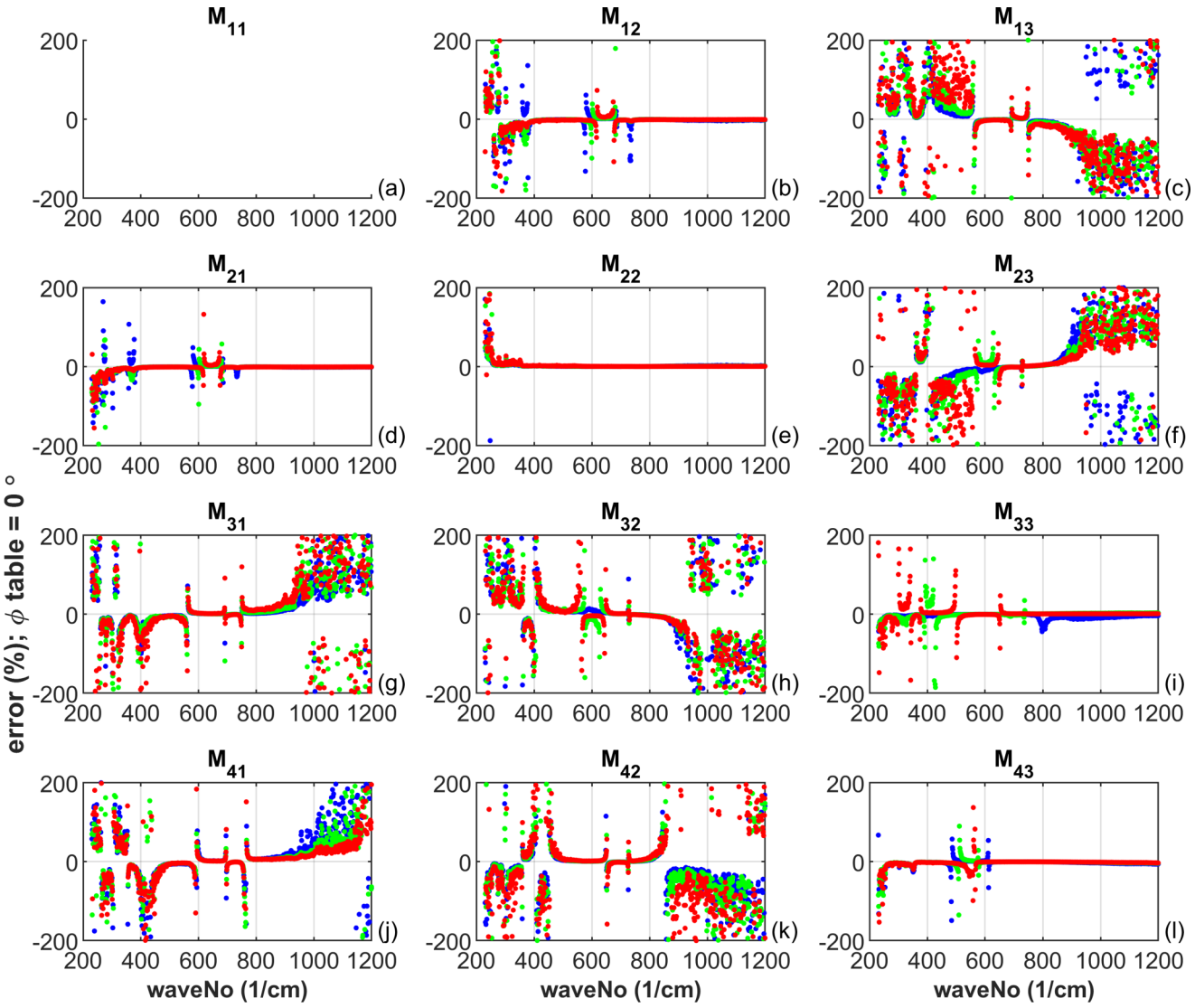

FIG. 2. Mueller matrix estimated experimental errors for the (010) crystal recorded and displayed for Mueller matrix elements indicated in the title of each subplot. Plot (a) is for M_{11} (normalized to unity), (b) is for M_{12}, (c) is for M_{13}, (d) is for M_{21}, (e) is for M_{22}, (f) is for M_{23}, (g) is for M_{31}, (h) is for M_{32}, (i) is for M_{33}, (j) is for M_{41}, (k) is for M_{42}, and (l) is for M_{43}. The red dots correspond to a 70° angle of incidence, the green dots to 60° angle of incidence, and the blue dots to 50° angle of incidence. Note that the estimated experimental errors are extremely large for many wave numbers ranging beyond the axis limitations of −200% to +200%. M_{22} is the best example from a set of 400–1200 wave numbers.

for wavenumbers greater than about 850 wavenumbers (1/cm) for 6 of 11 components of Mueller matrix measurements and for the *p*–*s* and *s*–*p* components of generalized, 4 out of 6. For wave numbers less than about 500 wave numbers (1/cm), the percent errors are extremely large for 10 out of 11 matrix spectra with a few exceptions in the narrow bands. The same is true for 4 out of 6 of the generalized measured spectra, specifically for the *p*–*s* and *s*–*p* components. The only low percent error Mueller spectrum is the M_{22} component and the *p*–*p* spectra of the generalized data. We do not see a correspondence to the location of modes Therefore, we choose to work with the *p*–*p* data for their accuracy.

C. Solutions

The solution strategy is to work at one wavenumber at a time. We repeatedly compute individual solutions using the Berreman formalism to obtain the four components of the monoclinic (*x*–*y*) subset of the ε tensor from sets of four different pairs of

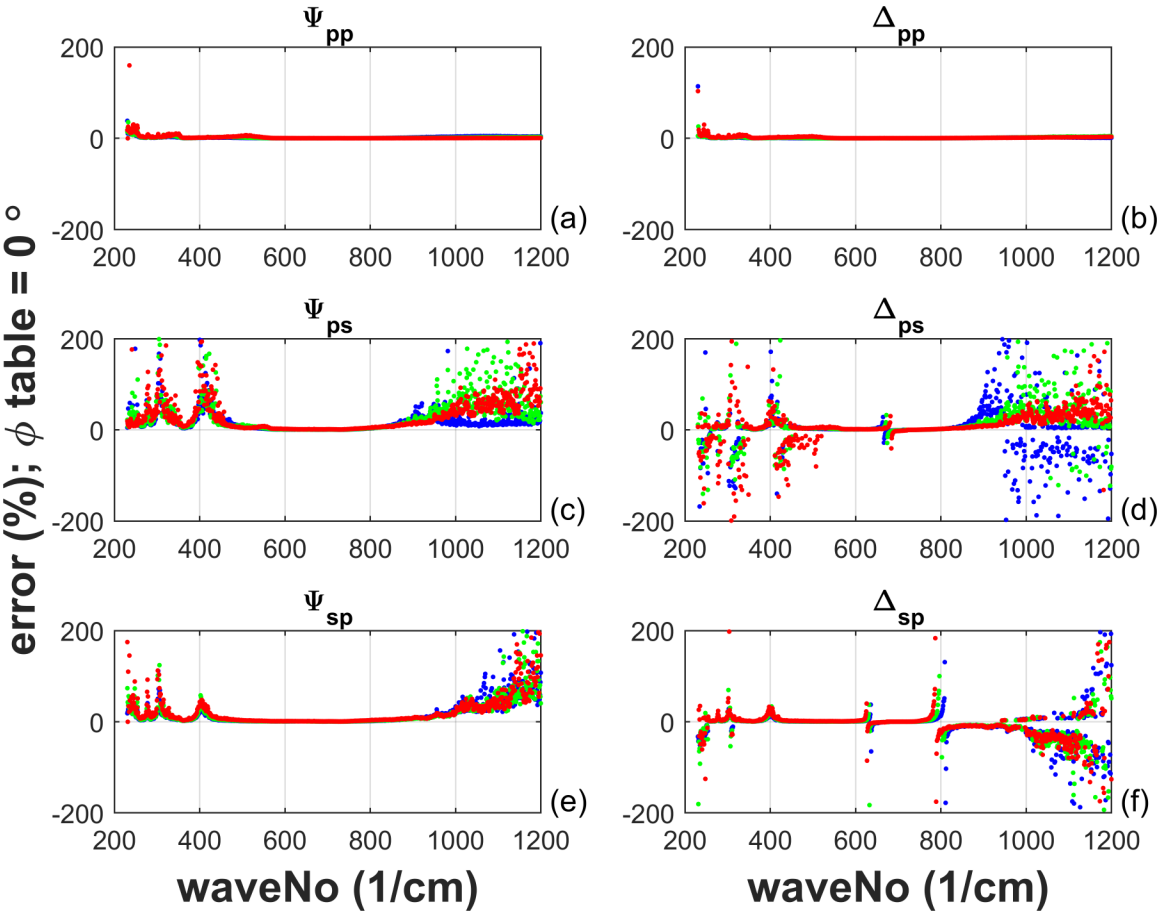

FIG. 3. Generalized estimated experimental errors recorded for the (010) crystal and displayed for Ψ and Δ as indicated in the title of each figure. Plot (a) is for Ψ_{pp}, (b) is for Δ_{pp}, (c) is for Ψ_{ps}, (d) is for Δ_{ps}, (e) is for Ψ_{sp}, and (f) is for Δ_{sp}. The red dots correspond to a 70° angle of incidence, the green dots to 60° angle of incidence, and the blue dots to 50° angle of incidence. Note that the estimated experimental errors are one or two orders of magnitude lower for the *pp* terms and are extremely large for the *ps* and *sp* measurements for many wave numbers ranging beyond the access limitations of −200% to +200%.

generalized measurements, Ψ and Δ. Computations are carried out at each wavenumber using the trust-region dogleg algorithm. This algorithm has been selected from the ever-increasing numerical methods because it both finds a numerical solution and requires fewer measurements. Thus, it has the opportunity to show the fine structure in the permittivity spectra and at the same time allows a greatly reduced measurement time which is always useful in the speedup and added convenience of making measurements.[17,18] To give an overview, a set of nine complex measurements at a selected wave number is picked from which four are taken at a time for a total of 126 combinations. Each of these sets of four Ψ_{pp} and Δ_{pp} values is presented to the trust-region dogleg algorithm as eight real numbers. The algorithm finds values of the permittivity tensor of Eq. (2) at the selected wave number using Berreman derivations of the Maxwell equations to match within a function tolerance error of 10^{-6}. If there are between 20 and 40 solutions, these are recorded and the algorithm moves on to the next wave number. If there are fewer or more than between 20 and 40, the stopping condition of function tolerance is adjusted up or down accordingly by a factor of 1.1. Adjustments in the function tolerance continue until the target number of solutions falls between 20 and 40.

Each crystal orientation is solved independently. Error in the measurement sets gives rise to error in the individual solutions so that they are not identical but instead cluster together. If one or more of a group of four measurement errors is too great with respect to the stopping conditions, a solution for that set of four measurements may not be possible. This is further discussed below.

In order to compute measurement sets with the best estimated experimental accuracy, we use only Ψ_{pp} and Δ_{pp} taken from sets of generalized data drawn from the four different table rotations and three incidence angles available in this work for each crystal. The work here makes use of that to discover a method for selecting a near-minimal infrared measurement set for β-gallium oxide. Although here we use and investigate only Ψ_{pp}, Δ_{pp} pairs at selected

incidence angles and table rotations, it has proved possible to solve using the less accurately measured values of the Ψ_{ps}, Δ_{ps} and Ψ_{sp}, Δ_{sp} pairs. The resulting solution accuracies, as reported by the standard deviations of the solutions, may be significantly less accurate. Thus, the statistical measurement uncertainty shows by finding multiple solutions (between 20 and 40) and reporting the mean and standard deviations at each wavenumber.

We did not use software from the J. A.Woollam Co. for data analysis, and instead, we used public domain approaches to solve for the Jacobian conditions and the resulting best solutions of the epsilon tensor elements. We also did not consider the systematic error reported on measurements as recorded by the measurement instrumentation. Instead, we searched for data with the most trustworthy support, i.e., those with the smallest systematic error. Then these data were included in our search for the minimum set, while the error data were not further included into the evaluation. We did not evaluate the weighted error.

IV. RESULTS AND DISCUSSION

A. Reflection intensity

A fundamental requirement in obtaining useful measurements is that there is sufficient reflected light intensity to provide accuracy. Assuming an incident intensity of unity, we see reflected intensity for the (010) crystal in Fig. 4. To be clear, we are not measuring intensity but rather the ellipsometric parameters using reflections that are bright (intense) rather than reflections that are weak and closer to the noise floor.

An examination of Fig. 4 makes it immediately apparent that for the (010) crystal, the pp reflection and the ss reflections are

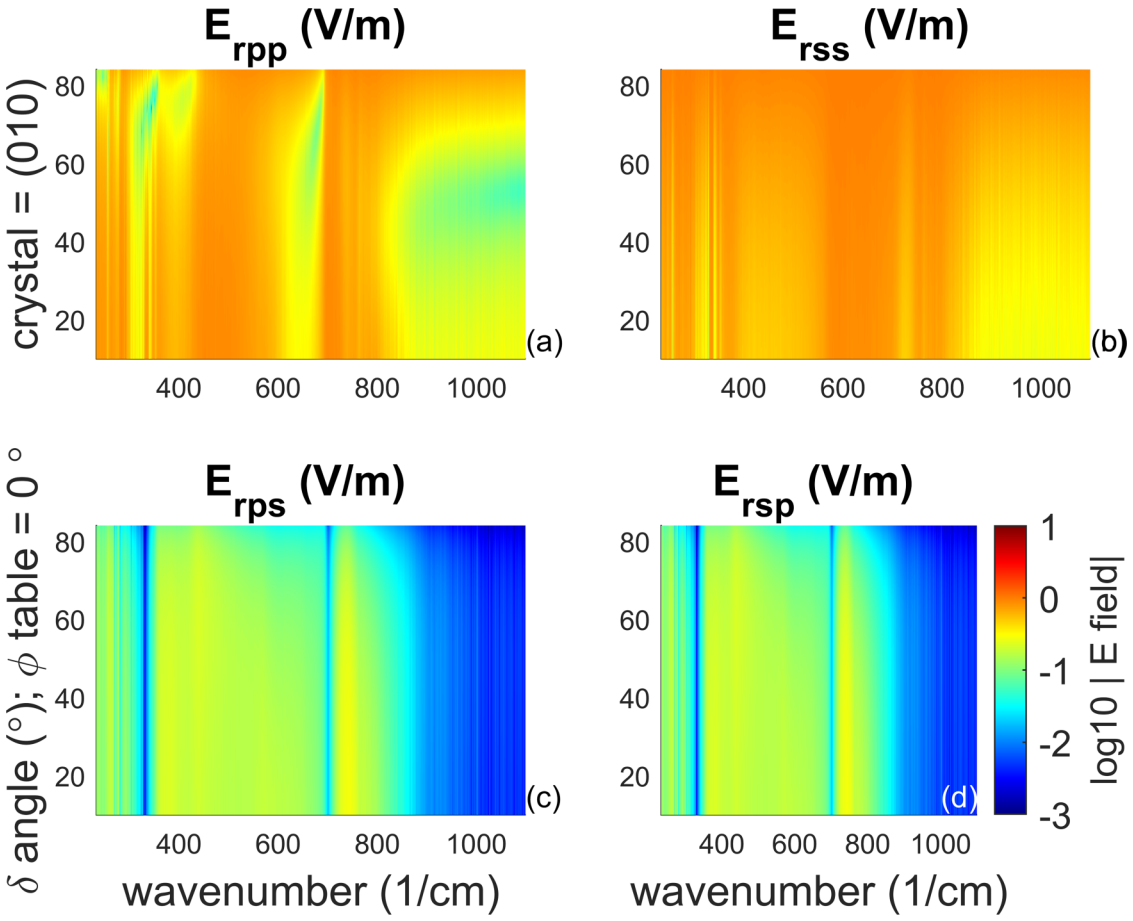

FIG. 4. Displays reflected intensities for the (010) crystal as a function of light incidence angle and wave number. For all four subplots, the intensity is represented by color with reference to the color bar on the far right. Bright red corresponds to a total reflectivity of 1 and dark blue corresponds to a reflectivity of 10^{-5}. (a) Exhibits the reflected intensity for an incident wave polarized in the p direction when the reflected wave is also detected polarized in the p direction. (b) Exhibits the reflected intensity for an incident wave polarized in the s direction and a reflected wave also polarized in the s direction. (c) Exhibits the reflected intensity for an incident wave polarized in the p direction and a reflected wave polarized in the s direction. (d) Exhibits the reflected intensity for an incident wave polarized in the s direction and a reflected wave polarized in the p direction.

orders of magnitude more intense than the ps and sp reflections, respectively. It is very interesting to compare this with Fig. 3. The importance of the intensity is as follows. While the instrument does not measure and report time-invariant intensity, it does make use of digital signals derived from light passing through time-varying optical elements. These elements modulate the light as a function of time and the light subsequently falls on detectors and is digitized. Even if the photodetector is perfectly linear across its dynamic range, what remains is digitization error arising because the range is equally divided by the number of bits in the analog to digital convertor. Thus, the effect of 1 bit of noise is much greater at the low end where the signal might be only a few bits versus at the high end of the range for which the signal is close to the full digital output, for example, $2^{16} = 65{,}536$ for a 16 bit A–D. Thus, the noise can be thousands of times greater for a low signal vs a high signal.

The high intensity pp and ss reflections are used to determine the measured Ψ_{pp} and Δ_{pp} values that have comparatively low estimated experimental errors. The low intensity *ps* and *sp* measurements, used to determine the values of Ψ_{ps}, Δ_{ps}, Ψ_{sp}, and Δ_{sp}, may be the reason that these parameters are very high in estimated experimental errors, as much as >200%. Recall that the estimated experimental error is reported by the measurement instrument at the same time as the measurements and are included in the machine-generated measurement data set. In addition, spectra for both intensity and error exhibit corresponding features, especially around 300 and 400 (1/cm). Another correlation between intensity and estimated experimental error appears from about 850 (1/cm) to 1200 (1/cm). This provides additional justification for selecting measurements at conditions that provide relatively intense reflections.

B. Measurement sensitivity

1. Real part of ε_{xx}

It is obvious that the permittivity must be sensitive to the measurements in order to be computed. Here, we define sensitivity as the derivative of the measured parameters, Ψ and Δ, with respect

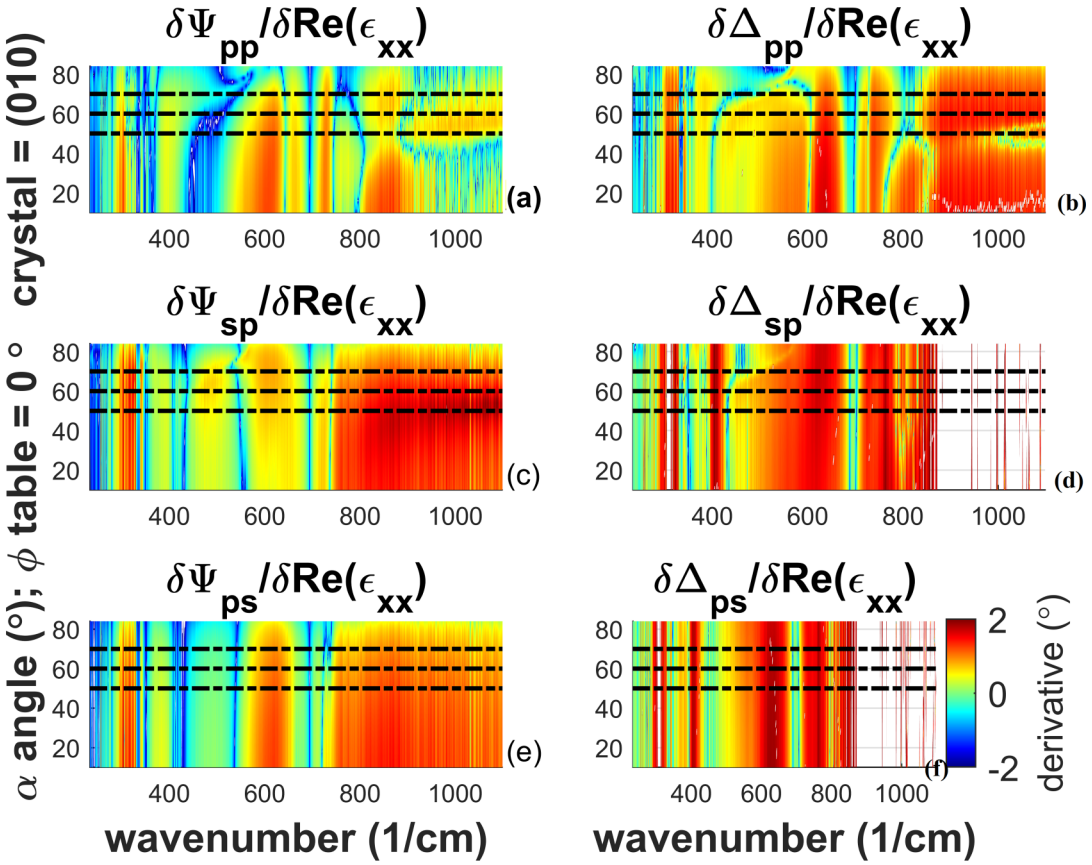

FIG. 5. Displays sensitivities for the (010) crystal for the three generalized Ψ and Δ measurements to the real part of the ε_{xx} component of the permittivity tensor at a table rotation of 0°. The horizontal dashed lines indicate the incidence angles used in the prior measurements, 50°, 60°, and 70°. Plot (a) shows the sensitivity in terms of $\log(abs(d\Psi_{pp}/d\ \mathrm{Re}(\varepsilon_{xx})))$ as a function of wave number (horizontal axis) and angle of incidence (vertical axis). Plot (b) is similar to (a) and exhibits $\log(abs(d\Delta_{pp}/d\ (\varepsilon_{xx})))$. Plot (c) exhibits $\log(abs(d\Psi_{sp}/d\ \mathrm{Re}(\varepsilon_{xx})))$, plot (d) exhibits $\log(abs(d\Delta_{sp}/d\ \mathrm{Re}(\varepsilon_{xx})))$, while plot (e) exhibits $\log(abs(d\Psi_{ps}/d\ \mathrm{Re}(\varepsilon_{xx})))$, and plot (f) exhibits $\log(abs(d\Delta_{ps}/d\ \mathrm{Re}(\varepsilon_{xx})))$.

to a single underlying permittivity parameter. This sensitivity applies at each wave number alone. The basic idea is that if a change in an underlying parameter, for example, in the real part of ε_{xx}, results in no change in Ψ and Δ, then the measurements of Ψ and Δ cannot provide for the determination of the real part of ε_{xx}. On the other hand, if a change in the real part of ε_{xx} gives rise to a large change in Ψ and Δ, these measurements may be used to determine the permittivity parameter.

The sensitivity is determined for each crystal across the incidence angle and wave number using computed approximations to the derivative obtained by making small changes to the permittivity parameters, computing the resulting changes in all six values of Ψ and Δ and then dividing them. Figure 5 shows, for the (010) orientation, the plots of generalized Ψ and Δ with respect to the real part of one of the permittivity tensor parameters, ε_{xx}. It is immediately evident that the sensitivities of these six parameters vary over a large range as a function of both wave number (the horizontal axis) and the light incidence angle (vertical axis).

Plots (a) and (b) in Fig. 5 are of primary interest in that they show regions of incidence-wavenumber space for the (010) crystal that are high and low in sensitivity, thus possessing sufficient intensity and sensitivity to allow a solution of the parameter of interest, Re(ε_{xx}). While plots (c)–(f) exhibit high sensitivity in many regions of the space, these are not useful because the intensities are very low.

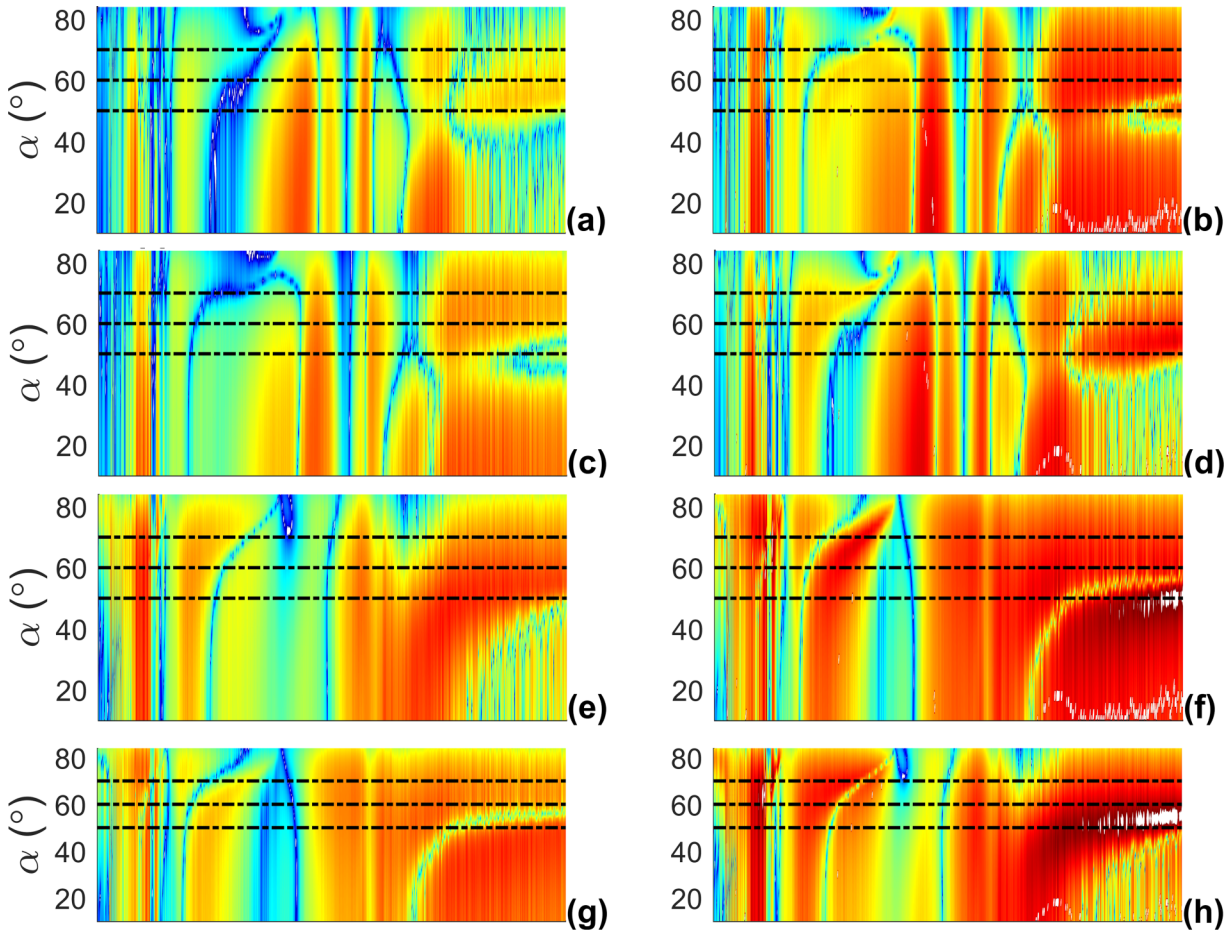

FIG. 6. Displays sensitivities for the (010) crystal for the three generalized Ψ_{pp} and Δ_{ss} measurements to all eight real valued components of the permittivity tensor, ε, at a table rotation of 0°. The horizontal dashed lines indicate the incidence angles used in the prior measurements: 50°, 60°, and 70°. Plots (a) and (b) show, respectively, the sensitivity of Ψ_{pp} and Δ_{ss} to the real part of ε_{xx}. Plots (c) and (d) show, respectively, the sensitivity of Ψ_{pp} and Δ_{ss} to the imaginary part of ε_{xx}. Plots (e) and (f) show, respectively, the sensitivity of Ψ_{pp} and Δ_{ss} to the real part of ε_{yy}. Plots (g) and (h) show, respectively, the sensitivity of Ψ_{pp} and Δ_{ss} to the imaginary part of ε_{xx}. Plots (i) and (j) show, respectively, the sensitivity of Ψ_{pp} and Δ_{ss} to the real part of ε_{zz}. Plots (k) and (l) show, respectively, the sensitivity of Ψ_{pp} and Δ_{ss} to the imaginary part of ε_{zz}. Plots (m) and (n) show, respectively, the sensitivity of Ψ_{pp} and Δ_{ss} to the real part of ε_{xy}. Plots (o) and (p) show, respectively, the sensitivity of Ψ_{pp} and Δ_{ss} to the imaginary part of ε_{xy}.

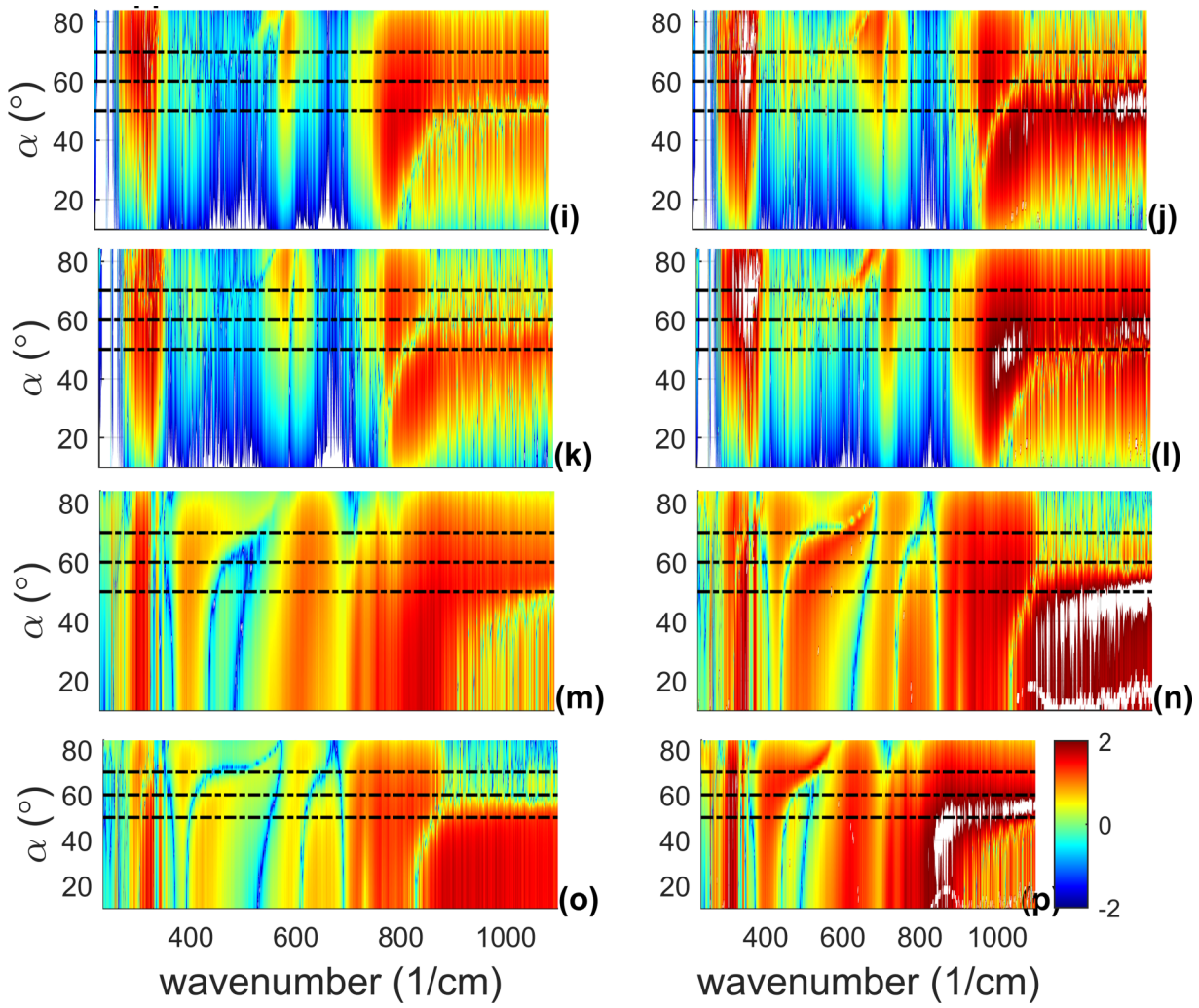

FIG. 6. (*Continued.*)

For improved visualization in Figs. 5 and 6, the upper limit of derivatives is set to $10^2 = 100$ in order to show four orders of magnitude more completely. Thus, the upper limit on the colorbar fully saturates at 2, log10(100), and the derivatives above are not shown in the form of any color but only as white, so white indicates a limit above 100.

2. Eight real valued components of ε

Figure 6 shows the sensitivities, Ψ_{pp} and Δ_{pp}, of all eight components of the crystal permittivity as determined by the (010) crystal.

An examination of Fig. 6 shows that for the (010) crystal, there is acceptable sensitivity except for ε_{zz}, for which the (−201) crystal is needed to be shown below. For ε_{zz}, the sensitivity is quite low across the range of wavenumbers for the Au modes. The sensitivity for all other components are good except for the occasional narrow vertical bands in the vicinity of particular wavenumbers.

3. Effect of table rotations

An inspection of measurement sensitivities at a table rotation of 0° in Fig. 6 leads to the necessity of rotating the crystal on the table to provide sufficient sensitivity across wavenumbers. Figure 7 shows just the effect of table rotation on the real part of ε_{xx} as showing all data here are impractical due to the number of figures required.

An examination of the plots in Fig. 7 reveals that at any given wave number, it is possible to have usable sensitivity to the real part of ε_{xx} simply by using measurements taken at different table rotations. This is also true for the imaginary part of ε_{xx} as well as

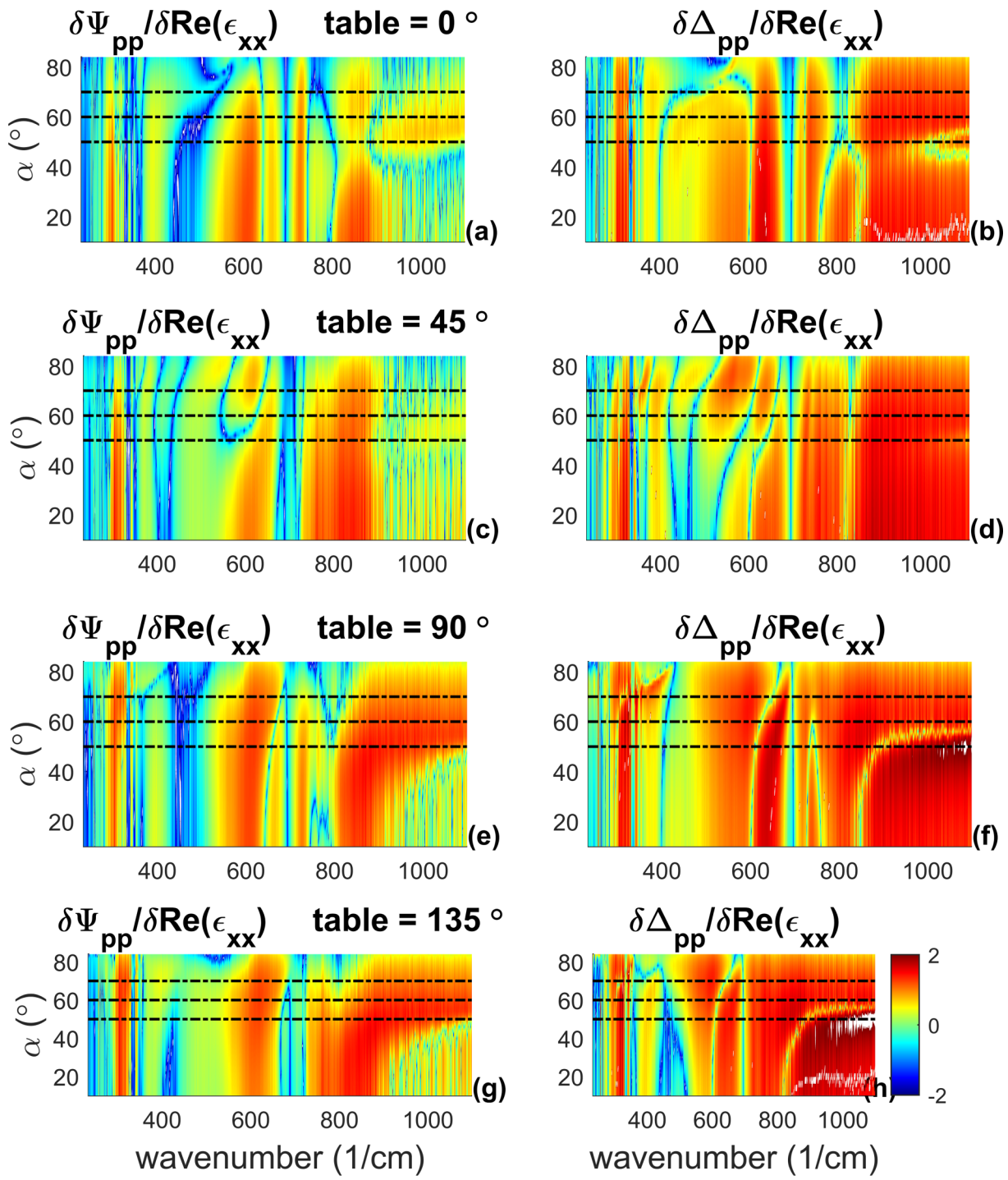

FIG. 7. Displays sensitivities for the (010) crystal for the three generalized Ψ_{pp} and Δ_{ss} measurements with respect to the real part of ε_{xx} at four different table rotations. The horizontal dashed lines indicate the incidence angles used in the prior measurements: 50°, 60°, and 70°. Plots (a) and (b) show, respectively, the sensitivity of Ψ_{pp} and Δ_{ss} to the real part of ε_{xx} at a table rotation of 0°. Plots (c) and (d) show, respectively, the sensitivity of Ψ_{pp} and Δ_{ss} to the real part of ε_{xx} at a table rotation of 45°. Plots (e) and (f) show, respectively, the sensitivity of Ψ_{pp} and Δ_{ss} to the real part of ε_{xx} at a table rotation of 90°. Plots (g) and (h) show, respectively, the sensitivity of Ψ_{pp} and Δ_{ss} to the real part of ε_{xx} at a table rotation of 135°.

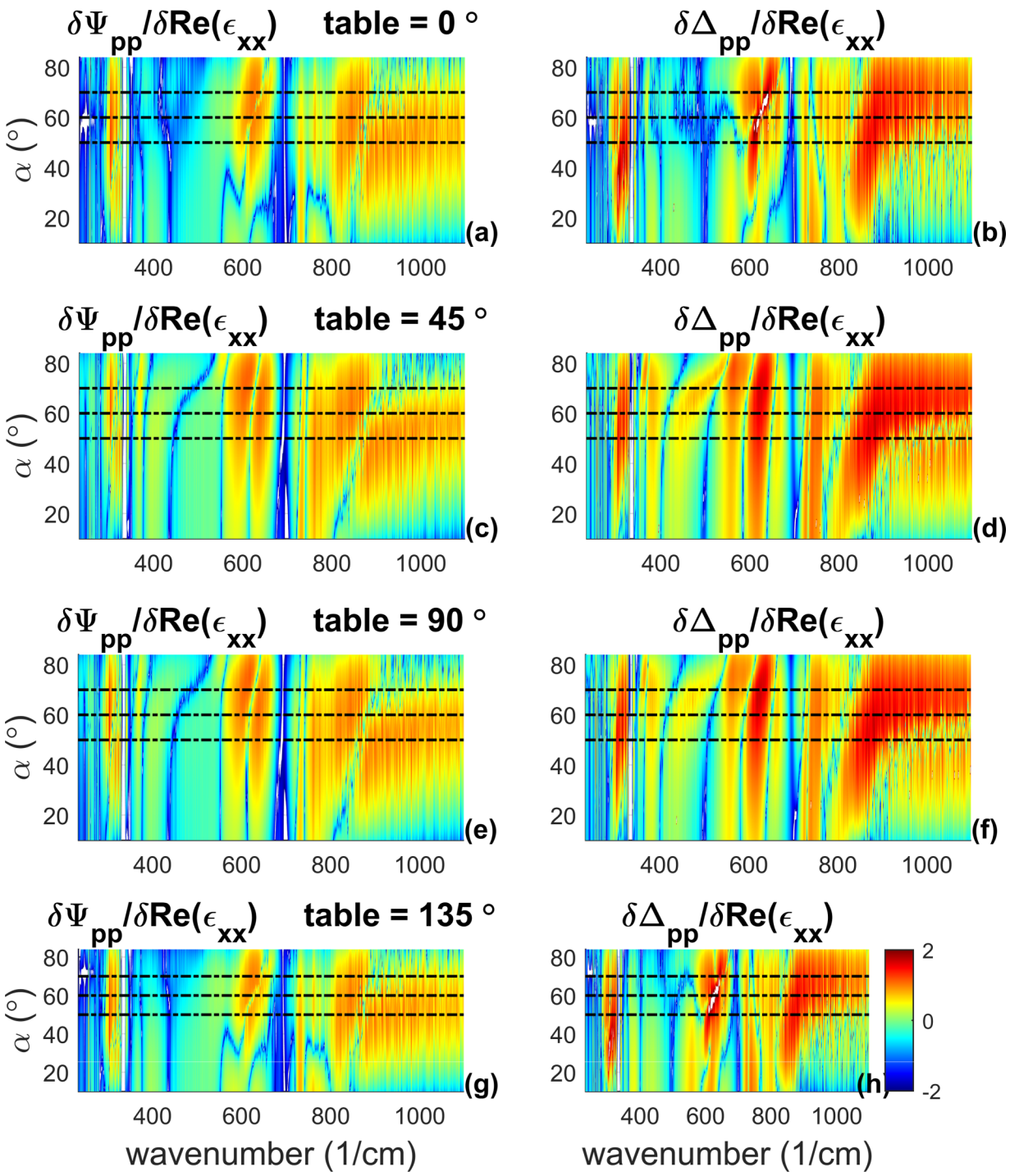

FIG. 8. Displays sensitivities for the (−201) crystal for the three generalized Ψ_{pp} and Δ_{ss} measurements with respect to the real part of ε_{zz} at four different table rotations. The horizontal dashed lines indicate the incidence angles used in the prior measurements: 50°, 60°, and 70°. Plots (a) and (b) show, respectively, the sensitivity of Ψ_{pp} and Δ_{ss} to the real part of ε_{xx} at a table rotation of 0°. Plots (c) and (d) show, respectively, the sensitivity of Ψ_{pp} and Δ_{ss} to the real part of ε_{xx} at a table rotation of 45°. Plots (e) and (f) show, respectively, the sensitivity of Ψ_{pp} and Δ_{ss} to the real part of ε_{xx} at a table rotation of 90°. Plots (g) and (h) show, respectively, the sensitivity of Ψ_{pp} and Δ_{ss} to the real part of ε_{xx} at a table rotation of 135°.

the real and imaginary parts of ε_{yy} and ε_{xy}. It is not true for ε_{zz} for reasons already mentioned resulting from the symmetry of the (010) crystal, and for this component, a separate, differently oriented crystal was used (−201).

Figure 8 displays the sensitivities of the (−201) face crystal corresponding to those reported in Fig. 6 for the (010) crystal.

First note that the sensitivities with respect to plots (a) and (b) shown in Fig. 8 are much greater than those for the same parameters shown in Fig. 6, plots (i) and (j) for the (010) crystal. This clearly demonstrates why the (010) crystal alone is insufficient to determine all values of the permittivity tensor. It is also evident that certain table rotations (45 and 90) do not provide high sensitivities.

C. Measurement condition considerations

This next criterion applies to groups of four individual complex measurements from which four complex equations arise through Maxwell's equations. At least these four complex, independent equations are needed to obtain solutions for the four components of the permittivity tensor.

In the vicinity of a known point consisting of eight real numbers, there exists a Jacobian matrix, which is an 8×8 matrix of all of the first-order partial derivatives of the equation parameters with respect to one another. Thus, it represents the differential at every point for which it is differentiable. Because it is square, its determinate provides information about the behavior of the system in transformations useful in the numerical methods employed here. A simple test of the Jacobian reveals the probability of achieving accurate solutions because it must be well conditioned to facilitate its use in the numerical process. The "condition number for inversion" or "condition number" is equal to the ratio of the largest to the smallest singular values of the Jacobian. A condition number near 1 indicates a well-conditioned matrix and larger values indicate increasingly ill-conditioned matrices.

At each wavenumber, combinatorics informs that there are 126 sets of four measurements taken from a total of nine. Figure 9 shows one set of conditions for all 126 measurement combinations taken at a wave number of 425.3 (1/cm). As can be seen, the condition varies significantly for each combination of four measurements.

Figure 10 shows the same data as Fig. 9 but sorted in order of increasing (worsening) condition. An examination of all 126 selection numbers does not reveal a distinctive pattern that is best for solving.

The condition also depends upon the wave number. Thus, Fig. 11 shows all 126 results for all 925 wave numbers measured for the crystal orientation (010). In this figure, the logarithm to the base 10 is represented by a color as shown in the color bar. Dark blue corresponds to an usable condition that fades to yellow as the highest condition number is displayed. White indicates conditions greater than $10^{3.5}$, considered to be essentially unusable. The vertical black lines indicate the B_u TO mode locations for β-gallium oxide for reference. Note that one vertical line through this figure corresponds to that in Fig. 9(a) at 425.3 (1/cm).

A number of interesting features are immediately evident in the figure. First note that each horizontal line corresponds to a selection of four measurements from the nine. It is evident that there are white lines and light-yellow ones extending across the entire wave number spectrum. This is very interesting as it demonstrates that a particular selection of measurements cannot be useful across all measured wave numbers. In addition, horizontal lines that are darker in color indicate useful measurement combinations. Thus, the figure identifies the measurements to include and to eliminate from the data set to streamline the measurement process.

Clearly, the condition is very dependent upon the selection of the four measurements. Thus, Fig. 11 shows all 126 results for all 925 wave numbers measured for the crystal orientation (010).

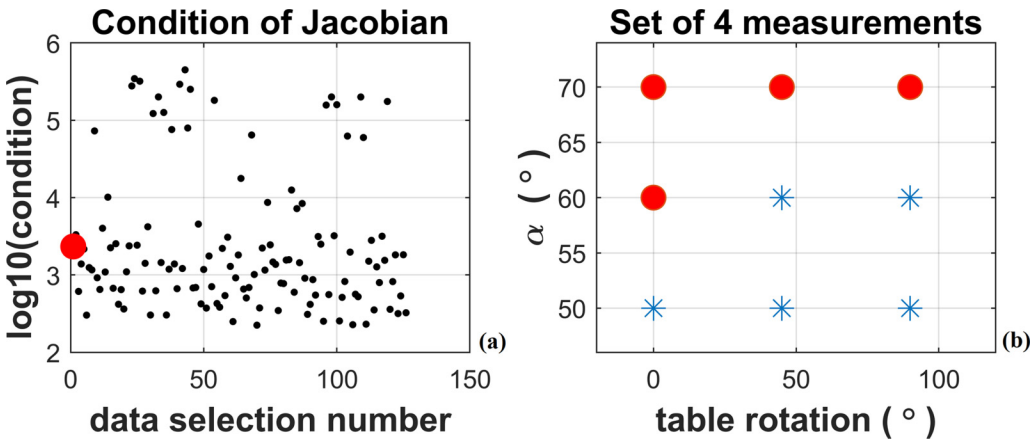

FIG. 9. Plot (a) displays the condition of each combination of measurements from 1 to 126 at a wave number of 425.3 (1/cm). The condition numbers vary greatly, so the value is plotted as the logarithm to the base 10 on the vertical axis. The red dot indicates the selection number that is displayed in plot (b), which shows red dots corresponding to the particular set of four numbers that is identified as selection one, plot (a). The blue asterisks show the points corresponding to the unused measurements.

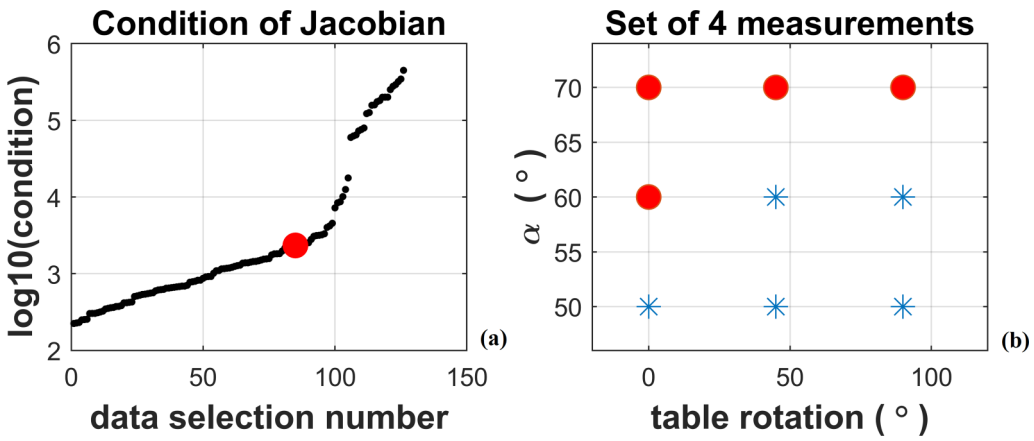

FIG. 10. Plot (a) displays the condition of each combination of measurements from 1 to 126 at a wave number of 425.3 (1/cm). The condition numbers vary greatly so the value is plotted as the logarithm to the base 10 on the vertical axis. The red dot indicates the selection number which is displayed in plot (b) which shows for red dots corresponding to the particular set of four numbers that identified as selection one, plot (a). The blue asterisks show the points corresponding to the unused measurements.

Figure 12 displays data obtained from the (−201) oriented crystal and otherwise handled in exactly the same way as in Fig. 10. It is very interesting to note that the condition for this crystal orientation is far less good than the condition for the (010) orientation. A consequence of this does appear to show up in the solution process for these two orientations. An examination of (−201) solutions in our prior work corresponds to a similar broad range of wave numbers in Fig. 12 also indicating a very poor condition for simultaneous solution.

The question then arises how the condition would be affected by adjustments to the table rotation or the incidence angle. Figure 13 shows such an adjustment, one of many, which shows the trend of what occurs when the difference between the table rotations is reduced. In this case, the table rotations are 40°, 45°, and 50° from the initial 0°, 45°, and 90° displayed in Fig. 11. Clearly, the condition has been made worse by closing up the steps between the table rotations. This trend was examined at other intermediate reductions in step size and the trend seen for intermediate values.

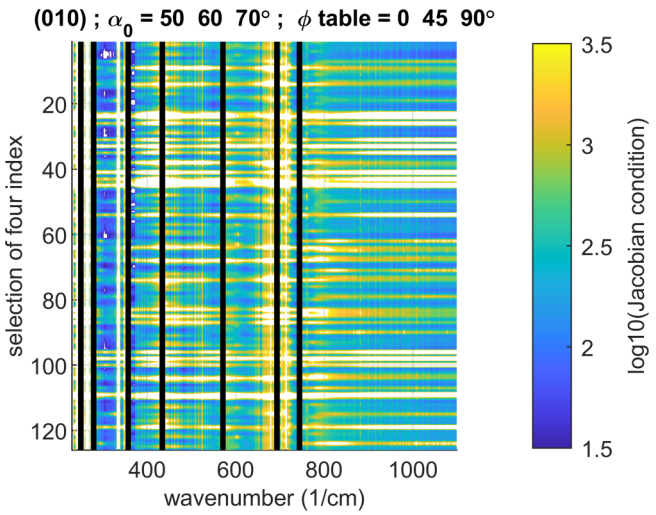

FIG. 11. Displays the condition at each pixel in the figure as indicated in the color bar that displays the logarithm to the base 10 of the condition of the pixel. The vertical axis corresponds to each of 126 measurement choices and the horizontal axis to each of 925 measured wave numbers. The vertical black lines correspond to the location of B_U modes for β-gallium oxide.

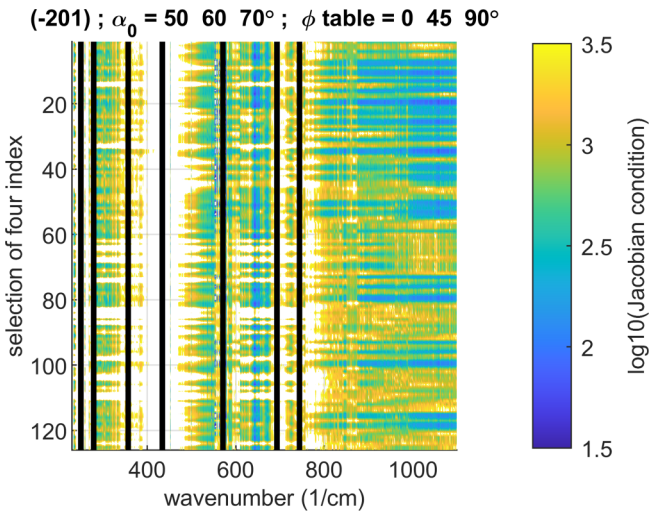

FIG. 12. Displays the condition at each pixel in the figure as indicated in the color bar that displays the logarithm to the base 10 of the condition of the pixel. The vertical axis corresponds to each of 126 measurement choices and the horizontal axis to each of 925 measured wave numbers. The vertical black lines correspond to the location of the B_U modes for β-gallium oxide.

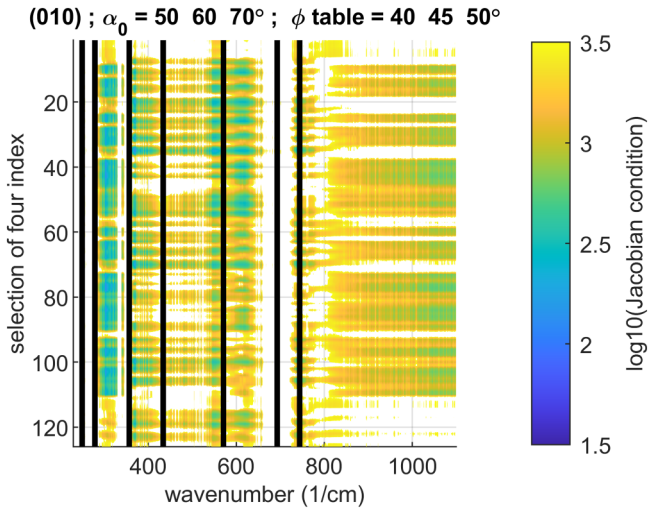

FIG. 13. Displays the condition at each pixel in the figure as indicated in the color bar that displays the logarithm to the base 10 of the condition of the pixel. The vertical axis corresponds to each of 126 measurement choices and the horizontal axis to each of 925 measured wave numbers.

Finally, we examine the effect of reducing the step size between incidence angles. Figure 14 shows one such experiment.

Again, in comparison with Fig. 11, it can be seen that reducing the step difference between incidence angles also causes the condition to get worse. Similar trends are seen for the (−201) crystal orientation not shown here.

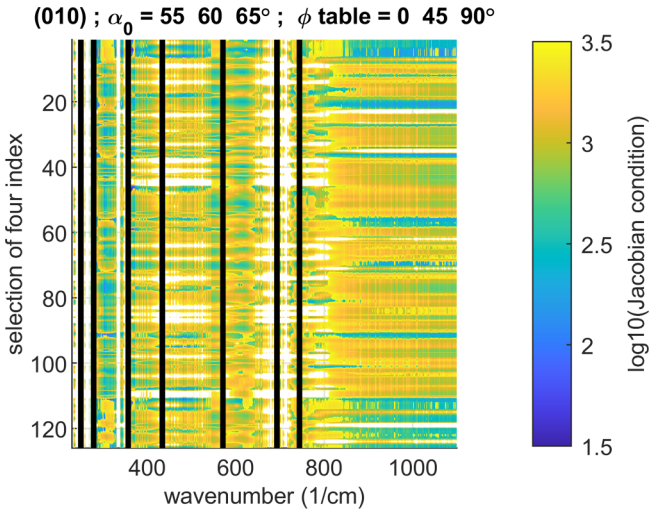

FIG. 14. Displays the condition at each pixel in the figure as indicated in the color bar that displays the logarithm to the base 10 of the condition of the pixel. The vertical axis corresponds to each of 126 measurement choices and the horizontal axis to each of 925 measured wave numbers.

From our investigation, we conclude that inclusion of data taken over a widespread range of table rotations is favorable over data taken at single or two table rotations only, and preferable over data taken that cover a large range of angles of incidence. In order to obtain the full permittivity tensor of a monoclinic crystal with all six unknowns, data need to be collected from a least two differently cut crystal surfaces, and for which a set of six near-minimum parameters need to be determined out of a near-minimum set of six measurement parameters; this is the subject of further investigations.

V. SUMMARY AND CONCLUSIONS

A method for determining a near-minimal set of measurements for solving for the four unknown ε tensor values for two monoclinic β-Ga_2O_3 crystals has been found. Thus, all tensor components can be determined. It is assumed that measurements will be made over a wide range of wave numbers and that the experimenter can control the orientation of the table and the incidence angles. In this work, results are obtained for two different crystal orientations, (010) and (−201). It is anticipated that exploring other crystal orientations may be helpful. The first step in this process is to determine at what measurement conditions (incidence angle and table rotation) there is a suitably strong reflection intensity that may allow accurate measurements to result. The method determines conditions for relative intensity for a given sample, while the intensity requirements for each ellipsometer will depend on its design. The next step is to examine the sensitivity of the unknown parameters to actual measurements. The purpose is to determine at what measurement conditions the parameters of interest, for which we are solving, are most sensitive to the measurements. Finally, because we are solving here for sets of four complex numbers that make up the permittivity tensor, we will require eight real number measurements readily provided by ellipsometry as Ψs and Δs. Along with Maxwell's equations, this set of measurements establishes the system of equations to be solved. Such solutions require that the equations, all eight of them, are reasonably independent. Dependent equations would result in no solution and the finding of a singularity. This is equivalent to trying to find the intersection of nearly parallel lines, which is made very difficult in the face of unavoidable measurement inaccuracy. Therefore, the final step is to examine the condition of the Jacobian matrices of the four complex number simultaneous equations to discover if they are well conditioned or poorly conditioned. All of these three steps taken together allow the determination of the sweet spot for measurements. Thus, as a consequence of carrying out these three steps, it is possible to greatly reduce the number of measurements required and at the same time improve the accuracy of the overall results.

This work is not driven by the need for making ellipsometry a faster exercise (by introducing certain speedy/genetic/smart/advanced data acquisition and/or analysis algorithms) but by the crucial fact that for low-symmetry crystals such as bGO, data acquisition protocols so far required weeks and months of nonstop measurements. The key here is to identify minimum sets of data, thus informing colleagues about ways to shorten precious measurement time, particularly in research environments where such materials are grown routinely to obtain, for example, next generation device materials and structures. This paper is about a clever selection of

where and what to measure for monoclinic materials rather than providing a general approach to make ellipsometry a faster exercise.

ACKNOWLEDGMENTS

Thanks are due to Tom Tiwald and James Hilfiker for many helpful discussions. This work was supported in part by the National Science Foundation (NSF) under Award Nos. NSF DMR 1808715 and NSF OIA 2044049, by Air Force Office of Scientific Research under Award Nos. FA9550-18-1-0360, FA9550-19-S-0003, and FA9550-21-1-0259, and by the Knut and Alice Wallenbergs Foundation award "Wide-bandgap semiconductors for next generation quantum components." Mathias Schubert acknowledges the University of Nebraska Foundation and the J. A. Woollam Foundation for financial support.

DATA AVAILABILITY

The data that support the findings of this study are available from the corresponding author upon reasonable request.

REFERENCES

[1]D. W. Berreman, J. Opt. Soc. Am. **62**, 502 (1972).
[2]P. Yeh, A. Yariv, and C.-S. Hong, J. Opt. Soc. Am. **67**, 423 (1977).
[3]P. J. Lin-Chung and S. Teitler, J. Opt. Soc. Am. A **1**, 703 (1984).
[4]M. Schubert, B. Rheinlander, J. A. Woollam, B. Johs, and J. Herzinger, J. Opt. Soc. Am. A **13**, 875 (1996).
[5]M. Schubert, Phys. Rev. B **53**, 4265 (1996).
[6]G. E. Jellison, Jr., M. A. McGuire, L. A. Boatner, J. D. Budai, E. D. Specht, and D. J. Singh, Phys. Rev. B **84**, 195439 (2011).
[7]M. Schubert *et al.*, Phys. Rev. B **93**, 125209 (2016).
[8]M. Higashiwaki, K. Sasaki, A. Kuramata, T. Masui, and S. Yamakoshi, Phys. Status Solidi A **211**, 21 (2014).
[9]M. Higashiwaki and C. M. Jessen, Appl. Phys. Lett. **112**, 060401 (2018).
[10]V. B. Mikhailik, H. Kraus, G. Miller, M. S. Mykhaylyk, and D. Wahl, J. Appl. Phys. **97**, 083523 (2005).
[11]A. Kato, S. Oishi, T. Shishido, M. Yamazaki, and S. Iida, J. Phys. Chem. Solids **66**, 2079 (2005).
[12]S. Cook, T. Rosenband, and D. R. Leibrandt, Phys. Rev. Lett. **114**, 253902 (2015).
[13]A. V. Turukhin, V. S. Sudarshanam, M. S. Shahriar, J. A. Musser, B. S. Ham, and P. R. Hemmer, Phys. Rev. Lett. **88**, 023602 (2001).
[14]A. I. Lvovsky, B. C. Sanders, and W. Tittel, Nat. Photonics **3**, 706 (2009).
[15]F. K. Urban III, D. Barton, and M. Schubert, J. Vac. Sci. Technol. A **38**, 023406 (2020).
[16]A. Kuramata, K. Koshi, S. Watanabe1, Y. Yamaoka, T. Masui, and S. Yamakoshi, Jpn. J. Appl. Phys. **55**, 12 (2016).
[17]C. B. Moler and G. W. Stewart, SIAM J. Numer. Anal. **10**, 241 (1973).
[18]M. J. D. Powell, "A hybrid method for nonlinear equations," in *Numerical Methods for Nonlinear Algebraic Equations*, edited by P. Rabinowitz (Gordon and Breach Science , New York, 1970), Chap. 6, pp. 87–114.